The 8th International Conference on Jets, Wakes and Separated Flows, ICJWSF-2024
September 23-25, 2024, Firenze, Italy

Reconstruction of a Continuous Flow Field from Discrete Experimental Data Points using Physics-Informed Neural Networks

Mattias E. G. Eck[1,*], Jakob G. R. von Saldern[2] Philipp zur Nedden[1]
Alessandro Orchini[3] and Christian Oliver Paschereit[1]

1: Chair of Fluid Dynamics, Technische Universität Berlin, Germany
2: Laboratory for Flow Instabilities and Dynamics, Technische Universität Berlin, Germany
3: Chair of Nonlinear Thermo-Fluid Mechanics, Technische Universität Berlin, Germany

1. Introduction

The efficiency of combustion processes within modern gas turbines strongly depends on fuel-air mixing, heat transfer mechanisms, and flame stability. To address these aspects and ensure a reliable flame anchoring, combustors comprise a swirler element which imprints a defined swirl on the air flowing through the burner [1, 2]. The thermal-flow mechanisms within swirl-stabilized flames have been extensively studied [2–5]. In this respect, and particularly in the context of novel carbon-free fuels which require fuel flexibility, the ability to actively vary the degree of swirl offers a significant advantage [3], as it can aid the in-depth investigation of different flames stabilized by the same burner. In this context, we have developed a novel burner concept capable of an active and continuous swirl variation [6]. The burner solely relies on fluidic actuation, i.e. the controlled injection of a secondary air mass flow, and allows to vary the flow regime from a non-swirled axial jet to a fully swirled flow. The underlying working principle has been first qualitatively demonstrated through numerical simulations and then experimentally validated through Laser Doppler Anemometry (LDA) [7]. While LDA was found to be a suitable technique to characterize the flow velocity profiles, it only acquires velocity data for sparsely distributed measurement points, and accurate LDA measurements require long data acquisition periods at each measurement position. As a result, the quality of LDA measurements is governed by a trade-off between the measurement time and the spatial resolution of the collected data points.

In this respect, this work demonstrates the potential of Physics-Informed Neural Networks (PINNs) to assimilate continuous flow fields from sparsely distributed LDA measurement points. For three different operation points, namely featuring no swirl, an intermediate degree of swirl, and a fully swirled flow regime, LDA experimental data was first acquired within discrete spatial measurement grids at various axial distances from the swirler's outlet. This data was then used to train PINN models, which yield a continuous flow field representation through the evaluation of Reynolds-Averaged Navier-Stokes (RANS) equations. A continuous function is produced which is differentiable within the entire flow domain, thus allowing for further analyses of the flow field, since the underlying physics (conservation of mass and momentum) is taken into consideration. The consideration of the physics is especially advantageous since it allows for the accurate reconstruction of all three velocity components characterizing the respective flow field. This aspect in particular will be exploited in the present work. The acquisition of the radial velocity component $\overline{u}_r$ has proven to be difficult due to its comparatively low values. Here we apply the PINN method to assimilate the radial velocity component based on the axial and tangential velocity components and the RANS equations. Additionally, for each operating point, the amount of training data used is systematically reduced while evaluating the physical validity of the computed flow field. As a result, the possibility to properly characterize a complex flow field through a minimum amount of required experimental training data is demonstrated.

2. Methodology

In this section we describe the setup used for the acquisition of the velocity data and the PINNs method.

2.1. Experimental Test Facility

The experimental data for the flow field characterization was acquired through LDA measurements under atmospheric and non-reacting conditions. Details on the test facility are schematically depicted in Fig. 1, and summarized in the following. Details and results can be furthermore found in [7]. The open test facility primarily

*Corresponding author: m.eck@tu-berlin.de

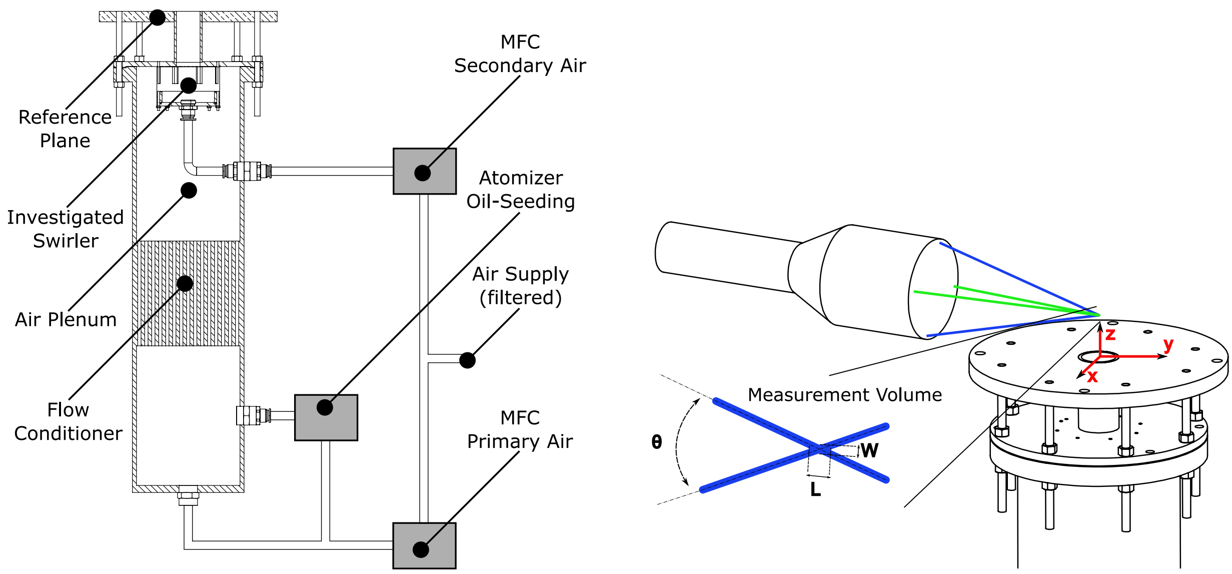

Fig. 1: Left: Experimental setup used to study the fluidic burner. Right: Schematic of the LDA setup.

consists of an air plenum connected to the fluidic burner. The primary air is led into the plenum through a filtered air supply, controlled by Mass Flow Controllers (MFCs). The secondary air is directly induced through a separate MFC. The primary air is infused with seeding particles through an apposite atomizer, needed for LDA measurements. The distributed particles have a median diameter of below 1 µm and it is assumed that the particle movement reliably resolves the flow. The average Reynolds number, based on the burner outlet diameter D, is kept constant at $Re \approx 10^5$, along with the total air mass flow $\dot{m}_{\text{tot}} = \dot{m}_{\text{p}} + \dot{m}_{\text{s}} \equiv 175\ \frac{kg}{h}$, amounting to a bulk velocity of $u_{\text{Bulk}} = 44.6\frac{m}{s}$. The Mass Flow Ratio MFR $= \frac{\dot{m}_{\text{s}}}{\dot{m}_{\text{p}}}$ between secondary and primary air, however, is varied to three operating points with three degrees of swirl, respectively: A non-swirled jet at MFR $= 6\%$, a flow subjected to an intermediate degree of swirl at MFR $= 10\%$, and a fully swirled flow at MFR $= 30\%$.

The employed 2D LDA system by *Dantec* relies on a two-color, four-beams laser system, featuring a 490 mW argon-ion laser by *Spectra-Physics*. Each of the colored beams is split in two, and one of each is led through a 40 MHz Bragg-Cell, where they are subjected to a frequency shift for directional sensitivity of the system. All four beams are then led through an integrated transmitting and receiving optic unit, which configures multiple beam parameters and simultaneously captures scattered and reflected light signals from seeding particles passing through the measurement volume. The focal length is set to $f = 310$ mm. For each emitted wavelength, the scattered light signals are processed through a photomultiplier, allowing for the simultaneous acquisition of two orthogonal velocity components in the Cartesian plane perpendicular to the laser-optic axis. The signal bursts are then analyzed in a Burst Spectrum Analyzer (BSA, Model *Dantec* BSA F60), which computes physical velocity values for each particle passing through the measurement volume within a given measurement time. For every measurement point, a velocity is inferred for each seeding particle (separately for each laser-/velocity-component), registered in a statistically significant amount of particle data within a given measurement time. A pronounced axial symmetry of the flow field downstream of the novel burner has been observed and demonstrated. In consequence, the experimental data used in this work could be advantageously acquired relying on measurements with a spatial location distribution following X-shaped grids, assuming an axisymmetric flow distribution. Here, the measurement locations are distributed along straight beams, aligned with the x and y coordinate axes for various constant axial distances z. In this regard, the used LDA setup can directly be used to acquire the respective tangential velocity components along one measurement point beam, the radial velocity components along the other, while acquiring the axial velocity for all measurement points. The use of X-shaped grids is found to be advantageous because it allows for a time-optimized assessment of the investigated flow field.

2.2. Physics-Informed Neural Networks

PINNs allow to approximate given data with a neural network and take physics constraints in the form of partial differential equations into account during network training [8]. As a result, the trained neural network approximates both the given data and a solution to a given set of equations. In the present work, PINNs are applied to reconstruct time-averaged LDA velocity fields and to approximate a solution of the RANS equations [9]. To this end, a neural network is set up that maps spatial coordinates to the mean flow quantities:

$$[\overline{\mathbf{u}}_\alpha,\, \overline{p},\, \nu_\alpha] = \mathbf{f}_\alpha(z, r), \tag{1}$$

where $\overline{\mathbf{u}}_\alpha = [\overline{u}_{\alpha,z},\, \overline{u}_{\alpha,r},\, \overline{u}_{\alpha,t}]$ is the mean velocity vector, $\overline{p}_\alpha$ is the mean modified pressure, ν_α is the eddy viscosity and z and r are the axial and radial coordinates. The neural network is denoted by $\mathbf{f}_\alpha$, where α represents the vector of trainable network parameters. These parameters are found by minimizing a composite loss function that constrains the PINN outputs to the measured data, physics equations, and additional boundary conditions:

$$\alpha = \text{argmin} \quad \mathcal{L}_{\text{data}} + \lambda_1 \mathcal{L}_{\text{physics}} + \lambda_2 \mathcal{L}_{\text{bc}}. \tag{2}$$

Here, λ_1 and λ_2 are weights that allow to shift the focus of network training between the individual constraints. The first term, $\mathcal{L}_{\text{data}}$, is the data loss term that penalizes deviations from the PINN output to available data points. In the present work, the measured axial and azimuthal velocities are used as training data:

$$\mathcal{L}_{\text{data}} = \frac{1}{N_z N_r} \sum_{i}^{N_z} \sum_{j}^{N_r} \left(\overline{u}_{\alpha,z}(z_i, r_j) - \overline{u}_z^*(z_i, r_j)\right)^2 + \left(\overline{u}_{\alpha,t}(z_i, r_j) - \overline{u}_t^*(z_i, r_j)\right)^2, \tag{3}$$

where the $*$-superscript denotes a measured quantity. N_z and N_r denote the total number of axial and radial measured locations which correspond to the number of measured planes and the number of measurement positions within each plane respectively. To evaluate the physics loss, the PINN output quantities are substituted into the RANS equations with the Boussinesq eddy viscosity model:

$$(\overline{\mathbf{u}}_\alpha \cdot \nabla)\overline{\mathbf{u}}_\alpha + \nabla \overline{p}_\alpha - \nabla \cdot \left[(\nu + \nu_\alpha)[\nabla \overline{\mathbf{u}}_\alpha + \nabla \overline{\mathbf{u}}_\alpha^T]\right] = \mathbf{e}_1, \tag{4a}$$

$$\nabla \cdot \overline{\mathbf{u}}_\alpha = \mathbf{e}_2, \tag{4b}$$

where $\mathbf{e}_1$ and $\mathbf{e}_2$ denote the residual of the RANS equations and the continuity equation, respectively. The residuals are evaluated at N_c discrete points sampled across the domain. The averaged residuals form the physics loss

$$\mathcal{L}_{\text{physics}} = \frac{1}{N_c} \sum_{i}^{N_c} ||r_i \mathbf{e}_1(z_i, r_i)||_2^2 + |r_i \mathbf{e}_1(z_i, r_i)|^2, \tag{5}$$

where the residuals are locally weighted with the radial coordinate to avoid division by zero. Similar to the data and the physics loss term, boundary conditions are implemented by adding a third loss term, $\mathcal{L}_{\text{bc}}$. The term enforces zero radial and tangential velocities on the symmetry axis, zero axial and tangential velocities for large radii, zero radial derivative of the axial velocity component on the symmetry axis, and no-slip boundary conditions on the upstream located wall. All constraints in Eq. (2) are taken into account in the form of deviations at discrete points in the cost function. However, the PINN is a continuous function which, once trained, can be evaluated at any point in space. In this work, network architectures with five layers of 20 neurons each are used. The *tanh* function is used as the activation function, and linear functions are used in the output layer.

3. Results

In this section, key features of the reconstructed flow fields are presented and discussed. First, the results are exemplary discussed for the operating point at MFR $= 30\%$, in which a fully swirled flow is observed (swirl number of $S \approx 0.9$). In this regard, a reference case is created, in which a PINN is trained with the maximum available quantity of training data. The training data consists of cylindrical velocity components (time averaged $\overline{u_z}$ and $\overline{u_t}$), experimentally acquired on X-shaped measurement grids over ten axial distances downstream of the outlet of the burner's mixing tube ($1 \leq z/D \leq 10$ with the outlet diameter D).

3.1. Reference Case Validation

The quality of the reference PINN model, trained with data from all available ten planes, is determined by the residual of the physics loss. In particular, we show in Fig. 2 its component related to the conservation of mass, the residual of Eq. (4b), which quantifies the local violation of the mass conservation within each cell of the domain. Since the PINNs rely on normalized input data, not comprising any physical dimension, the

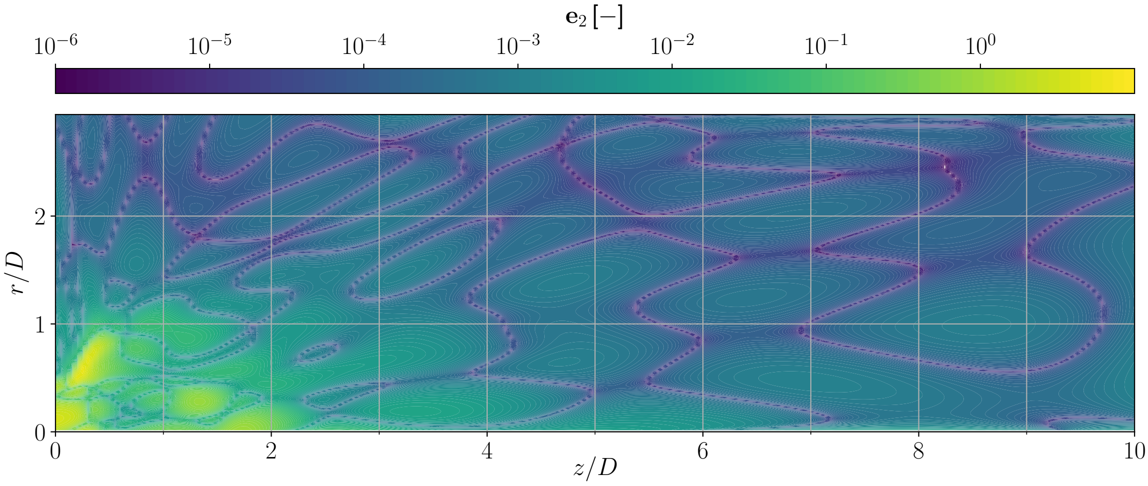

Fig. 2: Dimensionless residual of the physics loss concerning mass conservation for MFR = 30%, reference case with maximum amount of training data. As axial symmetry is assumed, the domain is shown as a half longitudinal section, where the left border at $z/D = 0$ represents the outlet plane of the burner's mixing tube (flow direction: left to right).

residuals are analogously dimensionless. At first, an area with a relatively large error is noticeable for $r/D \leq 1$ and $z/D \leq 1$. Here, the physical evaluation of the conservation of mass is confronted with a pronounced violation. Nevertheless, this area represents a relatively small portion of the evaluated domain and is furthermore located upstream of the first plane containing experimental training data, and downstream of the inflow boundary condition at $z/D = 0$. In combination with the high velocity gradients present close to the mixing tube outlet, the reconstructed flow field lacks robustness here. On the other hand, in the vast majority of the domain, for $z/D \geq 1$, the mass conservation error is extremely low, averaging less than 10^{-4}, validating the employed PINN approach for areas located downstream of the first training data plane.

3.2. Reconstruction of Radial Velocity Field

Having validated the PINNs approach, we now utilize it to study the flow fields stabilized by the fluidic burner. Fig. 3 shows the three cylindrical velocity components ($\overline{u_z}$, $\overline{u_r}$, and $\overline{u_t}$) for the reference case at MFR $=$ 30%, which features a high degree of swirl. The $\overline{u_z}$ component shows an area close to the mixing tube outlet, at $r/D \leq 0.5$ and $z/D \leq 2$, with a pronounced reversed flow amounting up to approximately 45% of the bulk velocity. This indicates the occurrence of a vortex breakdown creating a recirculation zone, as is the case for swirling flows stabilized by state-of-the-art swirl burners. This furthermore proves the ability of the employed PINN approach to reconstruct physically-relevant features of the flow. Close to the recirculation zone, a high tangential flow velocity is reconstructed, having the same order of magnitude as $\overline{u_z}$. For higher radial and axial distances, an increasing amount of air is entrained, enlarging the area of swirling fluid and simultaneously reducing $\overline{u_t}$.

As mentioned in § 1, the experimental acquisition of the radial velocity component $\overline{u_r}$ is found to be challenging with the chosen experimental approach, since the respective velocity magnitude strongly diverts from the other velocity components acquired simultaneously. As a result, $\overline{u_r}$ is not used to train the PINNs, but reconstructed by it. Hence, it is used as a parameter to assess the quality of the reconstructed flow fields. As visible from the reconstructed $\overline{u_r}$ depicted in the middle of Fig. 3, for axial distances $z/D \leq 1$, the trend complies well to the progression of $\overline{u_z}$ and $\overline{u_t}$. Air is entrained along the entire outer domain border, visible from a region of negative $\overline{u_r}$ for high radii. At the same time, the swirling jet expands, imprinting a positive $\overline{u_r}$ within the inner domain region, between $r/D \leq 1$ and $r/D \leq 2$ for high z/D. Towards the end of the domain for $z/D \to 10$, the swirling jet is completely expanded, and the radial air entrainment ceases with $\frac{\overline{u_r}}{u_{\text{Bulk}}} \to 0$. The physically-sound features confirm that the trained PINN model correctly reconstructs the radial velocity field from the axial and tangential velocity data measured in the experiments.

3.3. PINNs Training Optimization

One objective is to use PINNs to reduce the amount of experimental data, and thus the experimental time and resources, needed to characterize the flow. To this extent, we reconstruct the u_r velocity field from various

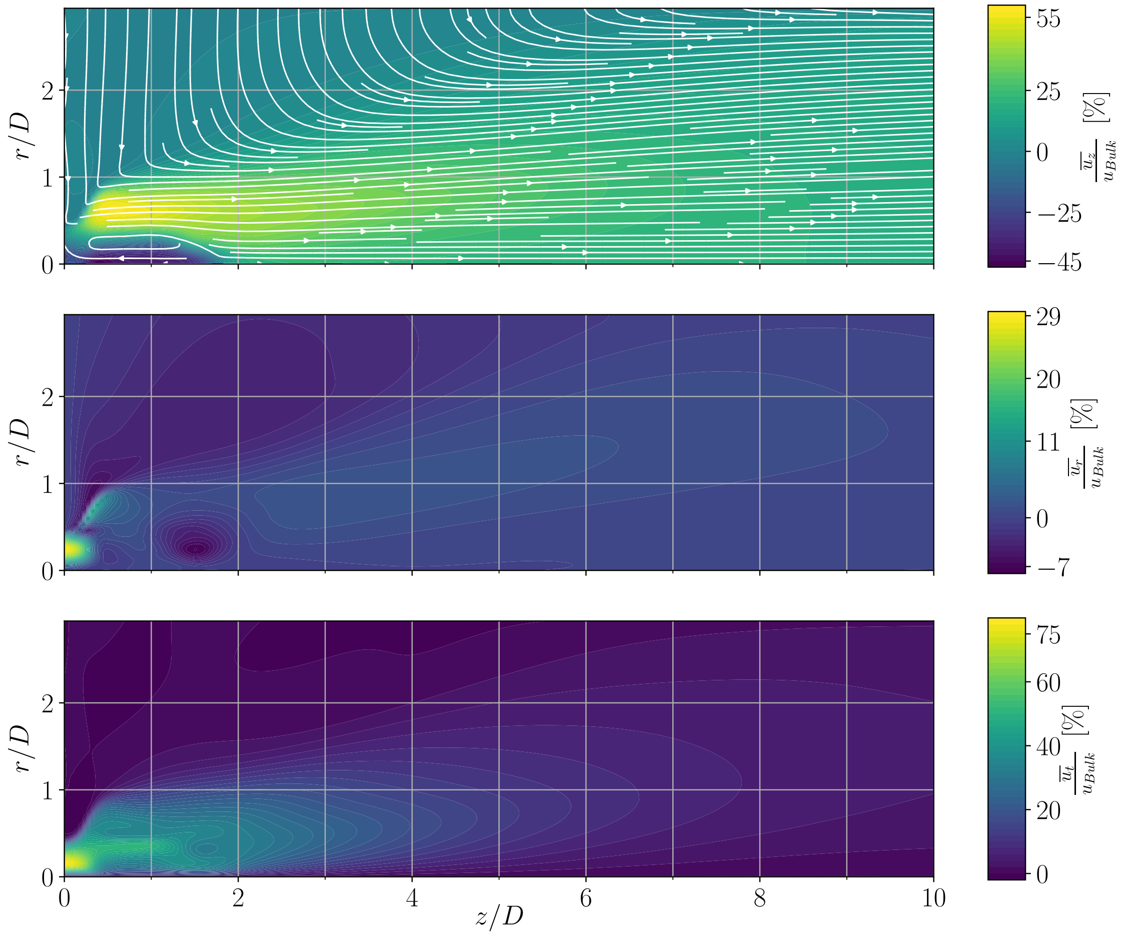

Fig. 3: Reconstructed velocity components $\overline{u_z}$ (top), $\overline{u_r}$ (middle), and $\overline{u_t}$ (bottom) for MFR = 30% at reference case. The white arrows in the top figure denote the streamlines of the reconstructed flow in the $r - z$ plane.

PINNs models trained with less data compared to the respective reference case. In particular, we use only the velocity data acquired on N of the ten available measurement planes. Then, a radial velocity error factor is computed via

$$U_{\text{r,error}} = \frac{\sum_{z/D \geq 1} |\overline{u}_{\alpha_{10},r} - \overline{u}_{\alpha_N,r}|}{u_{\text{Bulk}}}, \tag{6}$$

which compares the radial velocities reconstructed with less data to their respective reference case. This is repeated for three operating points with different MFR, thus swirl number. As discussed in § 3.1 and depicted in Fig. 2, the physics error within the reconstructed flow fields is maximized at axial distances upstream of the sampling location of the first training data ($z/D < 1$). Consequently, for the evaluation of the physical validity of the training data optimized PINNs, only information for $z/D \geq 1$ is considered. Fig. 4 depicts the progression of the calculated radial velocity error factor $U_{\text{r,error}}$ for all three operating conditions as N increases. For all operating conditions, a clear trend is visible: the divergence of the reconstructed radial velocity from the reference case monotonically decreases with increasing number of provided training data planes. The error magnitude, however, depends on the operating condition. The largest error is seen for MFR $= 30\%$, which has a high degree of swirl and, thus, creates a complex flow field with high velocity gradients and areas of reversed flow, as discussed in § 3. We note that the distribution of the planes chose to train the PINNs for $N < 10$ is not uniform. As N increases, more planes located at low z/D are employed, since for higher z/D the flow field is qualitatively similar to the operating points with no- and intermediate degree of swirl. Consequently, the error is harmonized between all operating points for $N \geq 6$, converging towards low levels between 0.05% and 0.12%.

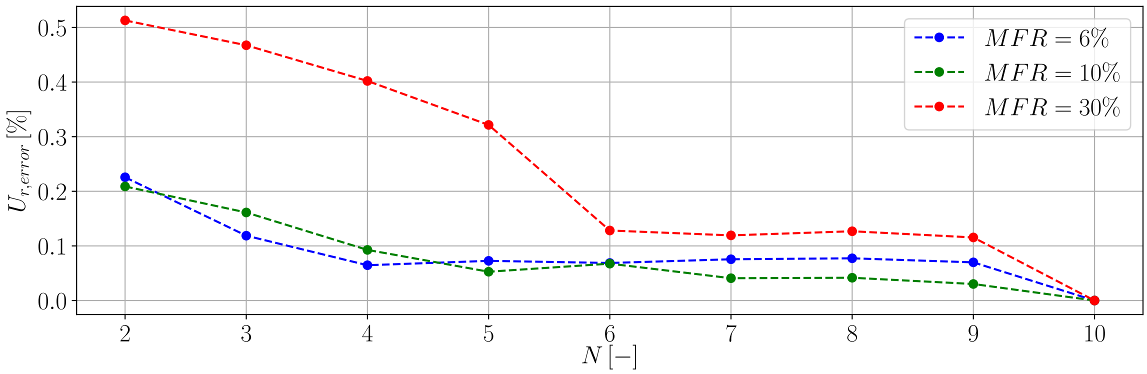

Fig. 4: Integrated error of radial velocity in % of the bulk velocity for all MFR cases. Data upstream of the first training plane is not considered.

4. Conclusions

A PINNs-based method for the reconstruction of continuous flow fields from sparse experimental data was presented. The method was tested on the flow fields generated by a novel burner concept, which allows for the active variation the flow's swirl number. For three operating conditions, with no, intermediate, and full swirl, respectively, experimental data consisting of three cylindrical velocity components was acquired and used to train PINN models. The suitability of the approach was validated, and reference cases were defined for the three operating conditions. The reconstructed flow field for one exemplary point was discussed in detail, and the divergence of the reconstructed radial velocity components between the reference and test cases was used to quantify the accuracy of PINNs trained with sparse data.

The work shows that the PINN method can be used to reconstruct flow fields with different characteristics, ranging form pure axial jets to fully swirled flows. Except for areas upstream of the first training data and close to the inlet boundary, the reconstructed fields are physically valid and are suitable for the continuous evaluation and characterization of the flow field. Furthermore, it was shown that a minimum amount of training data, at approximately six axial locations, is needed to yield accurate results, regardless of the operating point. PINNs hence have the potential to significantly reduce measurement expenses of complex measurement techniques and allow for the reconstruction of complex 3D flow fields from sparse data.

Acknowledgments

This work was funded by the European Research Council AdG HYPOTHESis, Grant ID. 101019937 and by the Deutsche Forschungsgemeinschaft (DFG, German Research Foundation) - 506170981. We thank Thorge Nissen for support with the computational calculations.

References

[1] J. D. Mattingly, H. Von Ohain, and J. A. Schetz. *Elements of Propulsion: Gas Turbines and Rockets*. AIAA, 2006.

[2] N. Syred and J. M. Beér. "Combustion in swirling flows: A review". In: *Combustion and Flame* 23 (1974), pp. 143–201.

[3] D. Durox, J. P. Moeck, J.-F. Bourgouin, P. Morenton, M. Viallon, T. Schuller, and S. Candel. "Flame dynamics of a variable swirl number system and instability control". In: *Combustion and Flame* 160 (2013), pp. 1729–1742.

[4] C. O. Paschereit, E. Gutmark, and W. Weisenstein. "Excitation of Thermoacoustic Instabilities by Interaction of Acoustics and Unstable Swirling Flow". In: *AIAA Journal* 38 (2000), pp. 1025–1034.

[5] G. Vignat, D. Durox, and S. Candel. "The suitability of different swirl number definitions for describing swirl flows: Accurate, common and (over-) simplified formulations". In: *Progress in Energy and Combustion Science* 89 (2022), p. 100969.

[6] M. E. G. Eck, P. M. zur Nedden, J. G. R. von Saldern, A. Orchini, and C. O. Paschereit. "Design of a Swirl-Stabilized Burner With Fluidically Variable Swirl Number". In: *Volume 3B: Combustion, Fuels, and Emissions*. ASME, 2023, pp. 1–10.

[7] M. E. G. Eck, P. M. zur Nedden, J. G. R. von Saldern, C. Peisdersky, A. Orchini, and C. O. Paschereit. "Experimental Design Validation of a Swirl-Stabilized Burner with Fluidically Variable Swirl Number". In: *Journal of Engineering for Gas Turbine and Power* (accepted) (2024).

[8] M. Raissi, P. Perdikaris, and G. E. Karniadakis. "Physics-informed neural networks: A deep learning framework for solving forward and inverse problems involving nonlinear partial differential equations". In: *Journal of Computational Physics* 378 (2019), pp. 686–707.

[9] J. G. R. von Saldern, J. M. Reumschüssel, T. L. Kaiser, M. Sieber, and K. Oberleithner. "Mean flow data assimilation based on physics-informed neural networks". In: *Physics of Fluids* 34 (2022), pp. 1–16.